

Common-reflection-surface-based prestack diffraction separation and imaging

P. Bakhtiari Rad*, B. Schwarz[†], D. Gajewski*, and C. Vanelle*

**University of Hamburg, Institute of Geophysics,*

Bundesstr. 55, 20146 Hamburg, Germany

†University of Oxford, Department of Earth Sciences,

South Parks Road, Oxford OX1 3AN, United Kingdom

(October 7, 2017)

Running head: **CRS-based prestack diffraction separation and imaging**

ABSTRACT

Diffraction imaging can lead to high-resolution characterization of small-scale subsurface structures. A key step of diffraction imaging and tomography is diffraction separation and enhancement, especially in the full prestack data volume. In this work, we consider point diffractors and present a robust and fully data-driven workflow for prestack diffraction separation based on wavefront attributes, which are determined using the common-reflection-surface (CRS) method. In a first of two steps, we apply a zero-offset based extrapolation operator for prestack diffraction separation, which combines the robustness and stability of the zero-offset CRS processing with enhanced resolution and improved illumination of the finite-offset CRS processing. In the second step, when finite-offset diffracted events are separated, we apply a diffraction-based time migration velocity model building which provides high-quality diffraction velocity spectra. Applications of the new workflow to 2D / 3D complex synthetic data confirm the superiority of the prestack diffraction separation over

the poststack method as well as the high potential of diffractions for improved time imaging.

INTRODUCTION

The seismic response of the earth comprises reflections and diffractions. While conventional seismic processing and imaging techniques over the past decades have been tuned to enhance reflections, the importance of diffractions has been recognized as well (see, e.g. Landa et al., 1987; Landa and Keydar, 1997; Moser and Howard, 2008). Diffractions carry valuable information about small-scale structures and heterogeneities, e.g., faults, pinch-outs, thin lenses or fractures and play a key role for high-resolution imaging of the subsurface features below the Rayleigh limit of half a seismic wavelength (Khaidukov et al., 2004).

A key step in diffraction imaging is the separation of diffractions from reflections since diffracted signals are usually masked by reflections and noise. Recently, different workflows for diffraction separation in the poststack domain were proposed (see, e.g. Fomel et al., 2007; Berkovitch et al., 2009; Reshef and Landa, 2009) to benefit from stability and data redundancy of zero-offset processing. However, diffraction separation in the full prestack data volume is of great importance in diffraction imaging which requires finite-offset processing. Finite-offset processing provides an improved resolution, especially in sparsely illuminated regions such as subsalt areas (Spinner et al., 2012). However, due to the larger number of finite-offset parameters, the problem is of higher dimensionality, which makes processing less stable and computationally more expensive than in the zero-offset setting especially in the case of large 3D data sets.

In this work, we present a workflow for prestack diffraction separation using wavefront attributes determined by the common-reflection-surface (CRS) method (see, e.g., Müller, 1999; Jäger et al., 2001). The 2D CRS-based poststack diffraction separation method was proposed by Dell and Gajewski (2011b). While diffractions in the poststack domain are

far easier to characterize and distinguish, our proposed workflow benefits from the stability of zero-offset CRS processing combined with the improved illumination of finite-offset processing to reliably separate diffractions from reflections and improve time imaging.

Zero-offset and finite-offset information is strongly coupled for diffractions (see, e.g. Berryhill, 1977). In order to establish a direct connection between zero-offset and finite-offset diffraction processing, we propose to employ the diffraction weighting function suggested by Dell and Gajewski (2011b) in the kernel of the partial CRS method introduced by Baykulov and Gajewski (2009) to generate a full prestack diffraction-only data volume without carrying out the computationally expensive generic finite-offset CRS method (Zhang et al., 2001). Since diffractions are usually masked by reflections and noise in the prestack domain, an advantage of the proposed workflow is that it benefits from the prestack data enhancement facility of the partial CRS method, leading to a significant increase in the signal-to-noise ratio of the diffraction-only data compared to the existing poststack approach.

In contrast to poststack diffraction separation, our scheme aims at making the full prestack diffraction response, with all its fine structure, available for further processing such as velocity analysis. To illustrate the benefit of separating the full prestack diffraction response, we apply time migration velocity analysis to prestack diffraction-only data in order to obtain the required migration velocities for subsequent imaging in time. This paper only considers diffraction from point-like structures, as even more complicated diffractors such as edges or wedges, from a kinematic viewpoint, contain a non-Snell scattering component that provides increased illumination (Bauer et al., 2016, 2017). For this diffraction component, the estimated stacking velocities are intrinsically dip-independent and can readily be used for prestack or poststack time migration (see, e.g., Sava et al., 2005; Fomel et al., 2007;

Berkovitch et al., 2009; Bakhtiari Rad et al., 2014).

Since a diffraction is inherently a 3D phenomenon, we also extend both post- and prestack diffraction separation workflows to 3D in order to overcome the problem of out-of-plane scatterers and compare their results. We focus on events from point diffractors in 3D. Finally, we evaluate the potential of diffractions for prestack time imaging by means of 2D and 3D complex synthetic data examples.

2D COMMON-REFLECTION-SURFACE STACK

The common-reflection-surface (CRS) method is a multiparameter stacking technique that, in contrast to the conventional common-midpoint (CMP) stack (Mayne, 1962) includes many neighboring CMPs. Consequently, the traveltimes moveout that needs to be determined for coherent summation for 2D acquisitions represents a surface rather than a curve. The hyperbolic 2D zero-offset CRS stacking operator can be derived from paraxial ray theory and, consequently describes traveltimes in a vicinity of a reference zero-offset ray (e.g. Schleicher et al., 1993). Parameterized in terms of the CRS wavefront attributes, it is given by (see, e.g., Jäger et al., 2001):

$$t_{\text{CRS}}^2(\Delta x_m, h) = \left(t_0 + \frac{2 \sin \alpha}{v_0} \Delta x_m \right)^2 + \frac{2 t_0 \cos^2 \alpha}{v_0} \left(\frac{\Delta x_m^2}{R_N} + \frac{h^2}{R_{\text{NIP}}} \right) \quad . \quad (1)$$

It describes the reflection traveltimes in the vicinity of the CMP location under consideration, x_0 , for deviations in midpoint, $\Delta x_m = x_m - x_0$, and half-offset, h , coordinates. In Equation 1, t_0 is the zero-offset traveltimes and v_0 is the near surface velocity. The three wavefront attributes or CRS parameters are, according to Hubral (1983), the incidence/emergence angle α at the coinciding central source and receiver locations, the radius

R_{NIP} of a fictitious wavefront emitted by a point source at the normal-incidence-point (NIP) on the reflector, and the radius R_{N} of a fictitious wavefront emitted by an exploding reflector element surrounding the NIP, the common-reflection-surface or CRS (see Figure 1).

[Figure 1 about here.]

2D diffraction

A diffractor can be described by a reflector segment with undefined orientation and infinite or, in practice, very high curvature, compared to the dominant seismic wavelength (e.g. Mann, 2002). The latter property implies that the common-reflection-surface shrinks into a point and thus, for diffractions $R_{\text{N}} = R_{\text{NIP}}$. Therefore, in the diffraction case, Equation 1 simplifies to (see, e.g., Dell and Gajewski, 2011b)

$$t_{\text{D}}^2(\Delta x_m, h) = \left(t_0 + \frac{2 \sin \alpha}{v_0} \Delta x_m \right)^2 + \frac{2 t_0 \cos^2 \alpha}{v_0 R_{\text{NIP}}} (\Delta x_m^2 + h^2) \quad (2)$$

In order to optimally apply Equation 2 for stacking, the separation of diffraction and reflection events has to be carried out prior to the stacking with the help of a diffraction separation criterion. This can be achieved by a comparison of the values for R_{N} and R_{NIP} . In practice, we find that for diffractions R_{N} will be close to R_{NIP} , but the values will in general not coincide exactly. Nevertheless, to ensure a reliable detection, we do not compare the values directly but by means of the function introduced by Dell and Gajewski (2011b),

$$W_{\text{D}} = \exp \left(- \frac{|R_{\text{N}} - R_{\text{NIP}}|}{|R_{\text{N}} + R_{\text{NIP}}|} \right) \quad . \quad (3)$$

The value of the function W_D becomes approximately equal to one if R_N is close to R_{NIP} , i.e., the event under consideration is most likely a diffraction. Otherwise, W_D becomes very small.

3D COMMON-REFLECTION-SURFACE STACK

Similar to the 2D version of the zero-offset CRS stacking operator, the 3D version can be derived from paraxial ray theory and, consequently, likewise is only valid, when the overburden heterogeneity (in particular laterally) is moderate. Expressed in terms of the CRS wavefront attributes, it can be written (Bergler et al., 2002)

$$t_{CRS}^2(\Delta \mathbf{x}_m, \mathbf{h}) = (t_0 + 2\mathbf{p}\Delta \mathbf{x}_m)^2 + 2t_0 (\Delta \mathbf{x}_m^T \mathbf{M}_N \Delta \mathbf{x}_m + \mathbf{h}^T \mathbf{M}_{NIP} \mathbf{h}) \quad , \quad (4)$$

where \mathbf{M}_{NIP} and \mathbf{M}_N are symmetric 2×2 matrices that describe the wavefront curvatures of the normal and normal-incident-point (NIP) waves, respectively. The slowness vector \mathbf{p} contains attributes of the emergence angle and azimuth of the central ray. The half-offset vector, \mathbf{h} , is the distance between shot and receiver, and $\Delta \mathbf{x}_m$ is the midpoint displacement vector with respect to the central ray coordinate. The zero-offset traveltime is t_0 .

3D point diffraction

Generally, diffractions have various shapes, since diffracting structures can have a directional (reflective) component for which Snell's law is partially satisfied. Therefore, it is common to distinguish between e.g. edge, wedge, tip or point diffractions (e.g. Klem-Musatov et al., 2008). In perfect correspondence with the 2D diffraction case discussed above, for a 3D event diffracted at a point-like discontinuity, the matrices of wavefront curvature become

identical, implying component-wise equality of the two. In this case, equation (4) can be simplified to (e.g. Dell and Gajewski, 2011a; Bakhtiari Rad et al., 2015)

$$t_D^2(\Delta \mathbf{x}_m, \mathbf{h}) = (t_0 + 2\mathbf{p}\Delta \mathbf{x}_m)^2 + 2t_0(\Delta \mathbf{x}_m + \mathbf{h})^T \mathbf{M}_{\text{NIP}}(\Delta \mathbf{x}_m + \mathbf{h}) \quad . \quad (5)$$

This equation represents the 3D CRS-based diffraction stacking operator. As mentioned in the previous section, for a point scatterer, the equality of the curvature matrices allows to identify the diffracted events and separate them from reflections. We extended the 2D diffraction weighting function to three dimensions without significant modifications:

$$W_D = \exp \left(- \sum_{i=0}^1 \sum_{j=0}^1 \frac{|M_N^{ij} - M_{\text{NIP}}^{ij}|}{|M_N^{ij} + M_{\text{NIP}}^{ij}|} \right) \quad , \quad (6)$$

where M_N^{ij} and M_{NIP}^{ij} are components of the corresponding matrices of the wavefront curvature. Again, like in the 2D case, if these components are close to each other, i.e., for point diffractions, W_D will be close to one. For reflections, the function value will be far from one.

WORKFLOW FOR PRESTACK DIFFRACTION SEPARATION

The partial CRS method (Baykulov and Gajewski, 2009) is used to sum up the finite-offset data coherently with a zero-offset-based CRS operator within an aperture expanded in both midpoint and half-offset coordinates without any further finite-offset CRS processing (Zhang et al., 2001). In the proposed method for prestack diffraction separation, the diffraction weight function initially evaluates for every zero-offset sample whether the sample belongs to a diffraction or not. If yes, partial stacking is carried out where only diffractions are considered. If not, the zero values are assigned to the according trace. Finally an enhanced prestack diffraction-only data volume is obtained. Prestack data enhancement is crucial

for prestack diffraction separation since diffractions are usually masked by noise because of their generally low amplitudes. In the following section, we summarize the different steps of our approach in a workflow.

In order to combine the features of the partial CRS method (Baykulov and Gajewski, 2009) with the wavefront attribute-based diffraction weighting function (Dell and Gajewski, 2011b,a), we suggest the following strategy for prestack diffraction separation and imaging:

1. Determination of the 2D / 3D CRS attributes using, e.g., the pragmatic search approach suggested by Müller (1999).
2. Evaluation of the separation criterion with proper choice of the separation threshold based on the complexity of the subsurface and data quality.
3. Execution of a partial CRS stack for diffractions with an optimal aperture in both half-offset and midpoint directions to generate diffraction-only gathers.

As soon as prestack diffraction-only gathers are available an automatic time-migration velocity estimation can be performed using coherency analysis with the semblance norm (Taner and Koehler, 1969). This automatic time migration velocity estimation provides dip-independent velocities that are immediately suitable for prestack time migration of not only diffraction-only data but the full unseparated prestack data volume. Initially, an automatic velocity scan from low to high velocities is performed, evaluating the semblance based on focusing of diffractions. The output is a coherence section that is suitable for picking time migration velocities. Finally, the migration velocity model is obtained by interpolation between picked locations. This procedure is automatically carried out for all CMPs. The workflow is therefore fast and robust even in the case of large 3D prestack data sets and

does not need user interaction except for the choice of the threshold value and the size of apertures. Please note however, that conflicting dip situations and, more importantly, an irregular or generally sparse diffraction coverage can deteriorate the interpolation results, which in turn may lead to insufficient imaging of reflected energy. While in general both, reflected and diffracted contributions should be jointly considered in velocity model building in time and depth (e.g. Bauer et al., 2017), in order to better appreciate the advantages and disadvantages of the suggested scheme, the following examples consider the influence of reflections and diffractions separately.

EXAMPLES

In the following, we present a complex 2D and a complex 3D synthetic data example, where we show that our suggested workflow leads to reliable 2D and 3D prestack diffraction separation in areas of moderate degrees of heterogeneity. To illustrate the potential benefit of diffraction-only prestack data for further processing, we use the separated prestack diffraction response for conventional velocity analysis, where the output, in contrast to the reflection case, can directly be used for time migration.

2D example: Sigsbee 2A

In order to investigate the performance of the proposed workflow in 2D, we have chosen the Sigsbee 2A data set. It is a constant density acoustic synthetic data set developed by the SMAART JV consortium. It models the geologic setting found in the Sigsbee escarpment in the deep water Gulf of Mexico. Figure 2(a) displays the velocity model. The irregular boundaries of the salt body as well as faults cause strong diffractions. Two rows of point

diffractors make this data set ideally suited to investigate diffractions. The data were generated for a CMP interval of 11.43 m with a maximum fold of 87 and offsets up to 7932 m. Noise with a signal-to-noise ratio of 10 was added to the data. Figure 2(b) displays the zero-offset stacked section prior to diffraction separation. We have then carried out the existing poststack and the proposed prestack diffraction separation workflows with a very strict separation threshold of 0.9. Figure 3(a) and Figure 3(b) display the zero-offset stacked section after the post- and prestack diffraction separation, respectively. By comparison, it is evident that the prestack diffraction separation workflow leads to a better diffraction separation as well as an increased signal-to-noise ratio.

For a more detailed investigation we have chosen CMP 700 in the region where the strata and the salt body interfere. In Figure 4, we show CMP gather 700 and the corresponding prestack diffraction gather. The weak as well as strong diffractions were well separated, and the data is heavily enhanced.

[Figure 2 about here.]

[Figure 3 about here.]

[Figure 4 about here.]

[Figure 5 about here.]

[Figure 6 about here.]

Finally, an important application of the CRS-based prestack diffraction separation is automatic time migration velocity analysis that provides dip independent velocities suitable

for prestack time migration. We have therefore generated the velocity spectra resulting from applications before and after post- and prestack diffraction separation workflows for the same CMP discussed above, i.e., CMP 700. It is shown in Figure 5 and demonstrates that we can achieve higher coherence as well as better focusing by considering the prestack diffraction-only data. It is evident that the better diffractions are separated, the higher the quality of the velocity spectra obtained.

Figure 6 shows the three closeups of the time-migrated section of the Sigsbee 2A dataset before (left) and after (right) prestack diffraction separation, respectively. The locations of the closeups in the zero-offset section are indicated by the frames in Figure 2(b). Since the 2D and 3D CRS stacking operators both were derived from paraxial ray theory, we do not incorporate closeups of the subsalt region, but, similar as Dell and Gajewski (2011b) confine ourselves to the discussion of regions on the left and above the salt, where lateral heterogeneity is moderate. Please be aware that these restrictions generally apply to time imaging as a whole and are not exclusive limitations of the suggested scheme. All velocities used for diffraction-only time imaging were picked automatically in the improved prestack diffraction semblance panels as shown in Figure 5(c). We observe that the strong as well as weak diffractions are generally well-imaged, which validates the quality of the estimated time migration velocities as the result of proposed method for diffraction imaging. Moreover, reflections are suppressed and the signal-to-noise ratio is increased.

3D example: SEG/EAGE 3D salt model

In order to evaluate the performance of the workflow in 3D, we have chosen the SEG/EAGE 3D wide azimuth (WAZ) complex data set. The data were introduced by Sandia National

Library (SNL). It describes a complex salt body in the Gulf of Mexico (see Figure 7). The top-of-salt is rugged and generates different patterns of diffraction events. We chose a portion of the data over the salt body for processing with inline ranges from 94 to 286 and crossline ranges from 43 to 428. The bin size was $40 \times 20 \text{ m}^2$ in inline and crossline directions, leading to a maximum fold of 18. The offset ranges from 0 to 2680 m.

Figure 8(a) shows the zero-offset stacked section of crossline 300 from the center of the salt body prior to diffraction separation. As expected, it exhibits different diffraction patterns as well as conflicting dips, where diffractions and reflections intersect. The 3D CRS stacking method was applied to the data to obtain the wavefront attributes. Subsequently, the 3D workflows for post- and prestack diffraction separation were applied to the data. Figure 8(b) and Figure 8(c) display the zero-offset diffraction-only data after post- and prestack diffraction separation, respectively. For this data we used a threshold of 0.8 for diffraction separation because of the lower data quality. We observe that the diffracted events are better separated and that the data quality is also much more enhanced with the prestack diffraction separation compared to the poststack approach.

For further evaluation, we have chosen a time slice through the center of the data set at about 2.5 s TWT. Figures 9(a) and 9(b) display the zero-offset stacked section before and after prestacked diffraction separation, respectively. Although most of the diffracted energy is separated well, residual reflections might be still present in the data because of the lower separation threshold. Some gaps and terminations are present in both sections since conflicting dips are not considered in the workflow and thus, lead to difficulties in these regions. Figure 10 displays a CMP gather from inline 130 before and after prestack diffraction separation, respectively. By comparing the results, we confirm that indeed mostly diffractions are present in the separated prestack data and only few residuals of reflections

remain due to the choice of a lower threshold value.

Finally, we have again determined time migration velocities from the prestack diffraction-only data obtained in the previous step. Figure 11(a) and Figure 11(b) illustrate the corresponding velocity panels of two example CMPs on the two different lines, before and after post- and prestack diffraction separation. Despite the low quality of the data, e.g., the low fold, the low SNR and the short maximum offsets, we can observe that 3D prestack diffraction separation in general leads to higher coherency and improved focusing in the semblance panels, thereby reflecting the prestack data enhancement and regularization capabilities of the utilized partial CRS kernel.

Figure 12 displays prestack time migration results using velocities obtained before and after prestack diffraction separation for an arbitrary inline 130 and Figure 13 for a time slice at 2.5 s TWT. Please note that dip-corrected reflection-based stacking velocities, which can be considered a reasonable approximation of time-migration velocities, were used in the Figure 12(a) and 13(a). We observe that the top-of-salt is imaged well and the diffractions are generally better collapsed with the diffraction velocities (see Figures 12(b) and 13(b)). Some of these results are outlined by red arrows in the figure, suggesting that diffraction velocities can be a good supplement in regions where migration velocities are otherwise hard to obtain. However, diffraction-based imaging may fail and lead to blurred images in regions without enough diffractions (as one can see in the Figure 12 and 13). Conflicting dips and unfocused diffractions, due to more complex diffractor geometry than the point-type considered in this work, may also deteriorate 3D diffraction velocity model building and subsequent imaging.

[Figure 7 about here.]

[Figure 8 about here.]

[Figure 9 about here.]

[Figure 10 about here.]

[Figure 11 about here.]

[Figure 12 about here.]

[Figure 13 about here.]

DISCUSSION

For the CRS processing used in this work conflicting dips were not considered. In addition, CRS attributes were determined by the so-called pragmatic approach (see, e.g. Müller, 1999; Mann, 2002; Müller, 2003) and no subsequent attributes refinement was applied. For diffractions a careful handling of conflicting dips will lead to an increase of diffracted events in the processed data since the weak amplitudes of diffractions are often masked by reflections cutting through diffraction events. Considering conflicting dips combined with the determination of the CRS attributes by a global search method considerably improves the quality of the CRS attributes (see, e.g. Walda and Gajewski, 2017) and subsequently the prestack diffraction separation. In addition, one may think of alternative ways to utilize wavefront attributes for the separation of diffractions in the prestack domain. Likewise considering point diffraction, Bauer et al. (2016) suggested to utilize the fact that the diffraction traveltimes moveout is the same in the common-shot, the common-receiver, and

the zero-offset domain to construct accurate finite-offset (i.e. prestack) diffraction operators from zero-offset wavefront measurements.

Double-square-root (DSR) traveltimes expressions are better suited for diffractions than the hyperbolic CRS operator (see, e.g. Gelchinsky et al., 1999; Schwarz et al., 2014). The quality of the determined CRS attributes influences the success of the diffraction separation or any other application in processing and imaging using wavefront attributes. Several stacking operators providing CRS wavefront attributes are available, which were systematically analyzed recently (Schwarz and Gajewski, 2017; Walda et al., 2017). In this context one can consider the operator used in this work as an example candidate to determine wavefront attributes. However, any other operator out of the CRS family might be applied as well.

Although dynamic properties of various types of diffractions differ, their kinematic behavior remain the same (Keller, 1962; Berryhill, 1977; Klem-Musatov et al., 2008). The proposed workflow for diffraction imaging is based on the assumption of point diffractions. However, separation of the diffractions due to a more complex diffractor geometry than the point-type (e.g., edge and tip diffractions) is a challenge in 3D due to the azimuth dependency of, e.g. three dimensional edge diffractions (e.g. Klovov et al., 2011) and, hence is not yet considered in the workflow. The geometrical behavior, however, is reflected in the wavefront attributes and allows to distinguish these events from reflections. This will be investigated in another study. From a kinematic viewpoint, these more complicated directional 3D diffraction types can be thought of as composed of a directional reflective component that obeys Snell’s reflection law and a point-diffraction contribution that corresponds to non-Snell scattering. We argue it is this non-Snell scattering that encodes the unique kinematic properties that make diffractions a valuable supplement to the conven-

tionally favored reflected wavefield, including superior illumination that can be utilized in macro-velocity model building (e.g. Bauer et al., 2017).

Although we have shown time imaging results using migration velocities estimated using reflected and diffracted contributions separately, it needs to be stressed that in general the best results are to be expected by taking reflected and diffracted contributions jointly into consideration. As stressed by other authors as well (e.g. Moser and Howard, 2008), diffraction imaging and inversion should complement conventional reflection-based strategies, rather than replace them.

CONCLUSIONS

We have presented a fully data-driven time-domain workflow for prestack diffraction separation and imaging based on wavefront attributes determined by the common-reflection-surface (CRS) method. The proposed method combines the stability of zero-offset CRS processing with the improved illumination of finite-offset CRS processing. The finite-offset separation of diffracted events performed well, leading to reliable diffraction-only prestack sections with an enhanced signal-to-noise ratio and shows certain advantages over the existing poststack workflow. As it is known from partial CRS technique, the use of zero-offset attributes for finite-offset processing leads to reliable results. Furthermore, we have shown that time migration velocity model building based on diffraction-only data has a high potential for improve prestack time migration. The migration velocities determined from diffraction-only data are dip independent and are therefore directly applicable for post- and prestack time migration. The velocity analysis of prestack diffraction-only data led to well-focused spectra that allowed for a reliable extraction of velocities. The promising results on 2D / 3D complex data sets reveal the high potential of prestack diffraction data

for improved time imaging.

ACKNOWLEDGMENTS

We thank the members of the Applied Seismics Group Hamburg for continuous discussions and support. Comments by Sergius Dell and Mikhael Baykulov are appreciated. We also thank the anonymous reviewers for their fruitful comments and suggestions. Special thanks go to J. Mann and N.A. Müller for providing 2D / 3D common-reflection-surface stack codes. Seismic Un*x routines were used for the generation of the figures. The Sigsbee 2A synthetic data were generated by the Subsalt Multiples Attenuation and Reduction Technology Joint Venture (SMAART JV). The SEG/EAGE 3D synthetic data were produced by the Sandia National Laboratories (SNL). This work was partially supported by the sponsors of the WIT consortium. The second author is supported by a research fellowship of the German Research Foundation (DFG, SCHW 1870/1-1).

REFERENCES

- Bakhtiari Rad, P., D. Gajewski, and C. Vanelle, 2015, 3D time migration velocity model building using CRS-based pre-stack diffraction separation: 85th Annual International Meeting, SEG, Expanded Abstracts, 4091–4095.
- Bakhtiari Rad, P., B. Schwarz., C. Vanelle., and D. Gajewski., 2014, Common reflection surface (CRS) based pre-stack diffraction separation: 84th Annual International Meeting, SEG, Expanded Abstracts, 4208–4212.
- Bauer, A., B. Schwarz, and D. Gajewski, 2016, Enhancement of prestack diffraction data and attributes using a travelttime decomposition approach: *Studia Geophysica et Geodaetica*, **60**, 1–16.
- , 2017, Utilizing diffractions in wavefront tomography: *Geophysics*, **82**, R65–R73.
- Baykulov, M., and D. Gajewski, 2009, Prestack seismic data enhancement with partial common-reflection-surface (CRS) stack: *Geophysics*, **74**, V49–V58.
- Bergler, S., P. Hubral, P. Marchetti, A. Cristini, and G. Cardone, 2002, 3d common-reflection-surface stack and kinematic wavefield attributes: *The Leading Edge*, **21**, 1010–1015.
- Berkovitch, A., I. Belfer, Y. Hassin, and E. Landa, 2009, Diffraction imaging by multifocusing: *Geophysics*, **74**, WCA75–WCA81.
- Berryhill, A. W., 1977, Diffraction response for nonzero separation of source and receiver: *Geophysics*, **42**, 1158–1176.
- Dell, S., and D. Gajewski, 2011a, 3D CRS-attributes Based Diffraction Imaging: 73rd Conference and Exhibition, EAGE, Extended Abstracts, B019.
- , 2011b, Common-reflection-surface-based workflow for diffraction imaging: *Geophysics*, **76**, S187–S195.

- Fomel, S., E. Landa, and M. T. Taner, 2007, Poststack velocity analysis by separation and imaging of seismic diffractions: *Geophysics*, **72**, U89–U94.
- Gelchinsky, B., A. Berkovitch, and S. Keydar, 1999, Multifocusing homomorphic imaging part 1. basic concept and formulas: *J. Appl. Geoph.*, **42**, 229–242.
- Hubral, P., 1983, Computing true amplitude reflections in a laterally inhomogeneous earth: *Geophysics*, **48**, 1051–1062.
- Jäger, R., J. Mann, G. Höcht, and P. Hubral, 2001, Common-reflection-surface stack: Image and attributes: *Geophysics*, **66**, 97–109.
- Keller, J. B., 1962, Geometrical theory of diffraction: *Journal of the Optical Society of America*, **52**, 116–130.
- Khaidukov, V., E. Landa, and T. J. Moser, 2004, Diffraction imaging by focusing-defocusing: An outlook on seismic superresolution: *Geophysics*, **69**, 1478–1490.
- Klem-Musatov, K., A. Aizenberg, J. Pajchel, and H. Helle, 2008, Edge and tip diffractions: Theory and applications in seismic prospecting: SEG Geophysical Monograph Series Number 14.
- Klokov, A., R. Baina, and E. Landa, 2011, Point and edge diffraction in three dimensions: 73rd Conference and Exhibition, EAGE, Extended Abstracts, B023.
- Landa, E., and S. Keydar, 1997, Seismic monitoring of diffraction images for detection of local heterogeneities: *Geophysics*, **63**, 1093–1100.
- Landa, E., V. Shtivelman, and B. Gelchinsky, 1987, A method for detection of diffracted waves on common-offset sections: *Geophysical Prospecting*, **35**, 359–373.
- Mann, J., 2002, Extensions and applications of the common-reflection-surface stack method: PhD thesis, University of Karlsruhe.
- Mayne, W. H., 1962, Common reflection point horizontal data stacking techniques: *Geo-*

- physics, **27**, 927–938.
- Moser, T. J., and C. B. Howard, 2008, Diffraction imaging in depth: Geophysical Prospecting, **56**, 627–641.
- Müller, N.-A., 2003, The 3D Common-Reflection-Surface stack - theory and application: Master thesis, University of Karlsruhe.
- Müller, T., 1999, The common reflection surface stack method: Seismic imaging without explicit knowledge of the velocity model: PhD thesis, University of Karlsruhe.
- Reshef, M., and E. Landa, 2009, Post-stack velocity analysis in the dip-angle domain using diffractions: Geophysical Prospecting, **57**, 811–821.
- Sava, P. C., B. Biondi, and J. Etgen, 2005, Wave-equation migration velocity by focusing diffractions and reflections: Geophysics, **70**, U19–U27.
- Schleicher, J., M. Tygel, and P. Hubral, 1993, Parabolic and hyperbolic paraxial two-point traveltimes in 3D media: Geophysical Prospecting, **41**, 495–513.
- Schwarz, B., and D. Gajewski, 2017, The two faces of NMO: The Leading Edge, **36**, 512–517.
- Schwarz, B., C. Vanelle, D. Gajewski, and B. Kashtan, 2014, Curvatures and inhomogeneities: An improved common-reflection-surface approach: Geophysics, **79**, S231–S240.
- Spinner, M., C. Tomas, P. Marchetti, C. Gallo, and S. Arfeen, 2012, Common-offset CRS for advanced imaging in complex geological settings: 82nd Annual International Meeting, SEG, Expanded Abstracts, 1–5.
- Taner, M., and F. Koehler, 1969, Velocity-spectra digital computer derivation and applications of velocity functions: Geophysics, **34**, 859–881.
- Walda, J., and D. Gajewski, 2017, Determination of wavefront attributes by differential evolution in the presence of conflicting dips: Geophysics, **82**, V229–V239.

- Walda, J., B. Schwarz, and D. Gajewski, 2017, A competitive comparison of multiparameter stacking operators: *Geophysics*, **82**, 1–46.
- Zhang, Y., S. Bergler, and P. Hubral, 2001, Common-reflection-surface (CRS) stack for common offset: *Geophysical Prospecting*, **49**, 709–718.

LIST OF FIGURES

1	Physical meaning of the 2D zero-offset CRS wavefront attributes	24
2	Sigsbee 2A: the velocity model and the zero-offset section	25
3	Sigsbee 2A: diffraction-only data after post- and prestack diffraction separation.	26
4	Sigsbee 2A: CMP 700 before and after prestack diffraction separation . . .	27
5	Sigsbee 2A: velocity spectrum for CMP 700 before and after diffraction separation	28
6	Sigsbee 2A: time-migrated closeup section of full and diffraction-only data .	29
7	3D SEG/EAGE velocity model	30
8	3D SEG/EAGE model: crossline 300, post- and prestack diffraction separation results	31
9	3D SEG/EAGE model: Time slice at 2.5 s. prestack diffraction separation result	32
10	3D SEG/EAGE model: results for a CMP gather	33
11	3D SEG/EAGE model: velocity spectra for two example CMP gathers from the two different lines	34
12	3D SEG/EAGE model: prestack time migration results for inline 130	35
13	3D SEG/EAGE model: prestack time migration results for time slice 2.5 s .	36

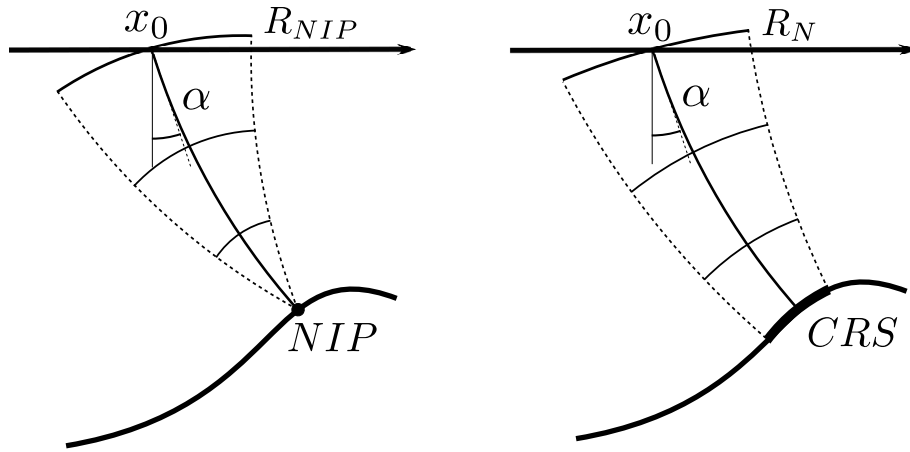
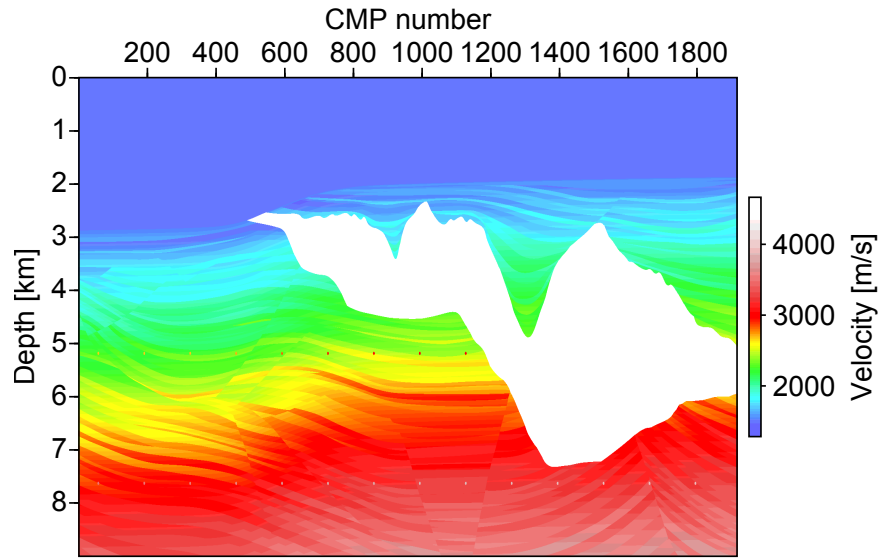
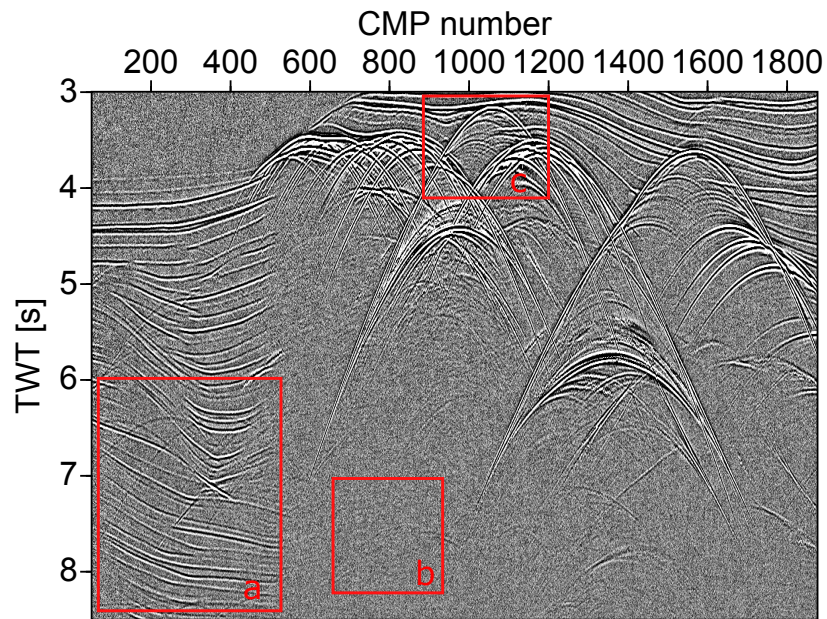


Figure 1: Physical meaning of the 2D zero-offset CRS wavefront attributes (Hubral, 1983): (left) R_{NIP} is the radius of curvature of a wavefront emitted by a fictitious point source at the normal incidence point (NIP); (right) R_N is the radius of wavefront curvature of the fictitious so-called normal wave emitted by an exploding reflector element, the common reflection surface (CRS). The incidence angle is denoted by α .

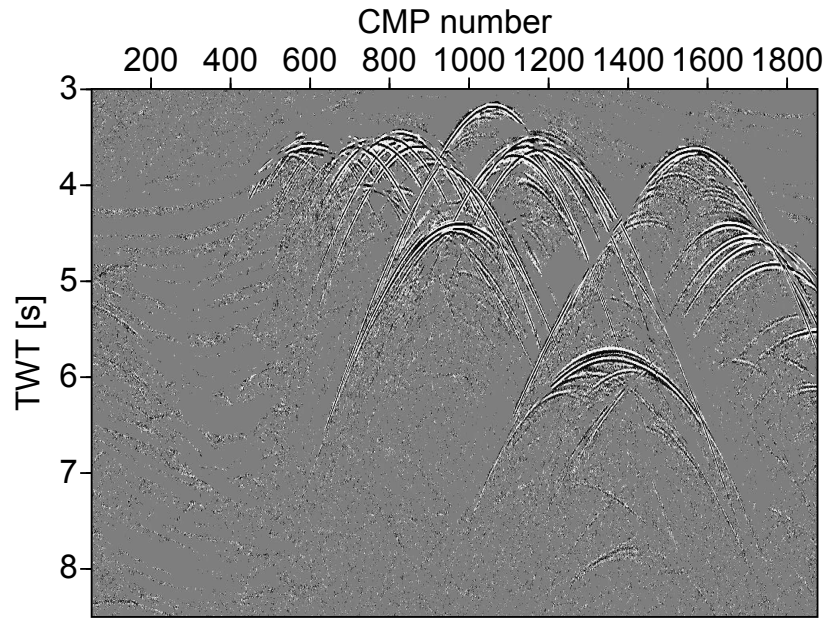


(a)

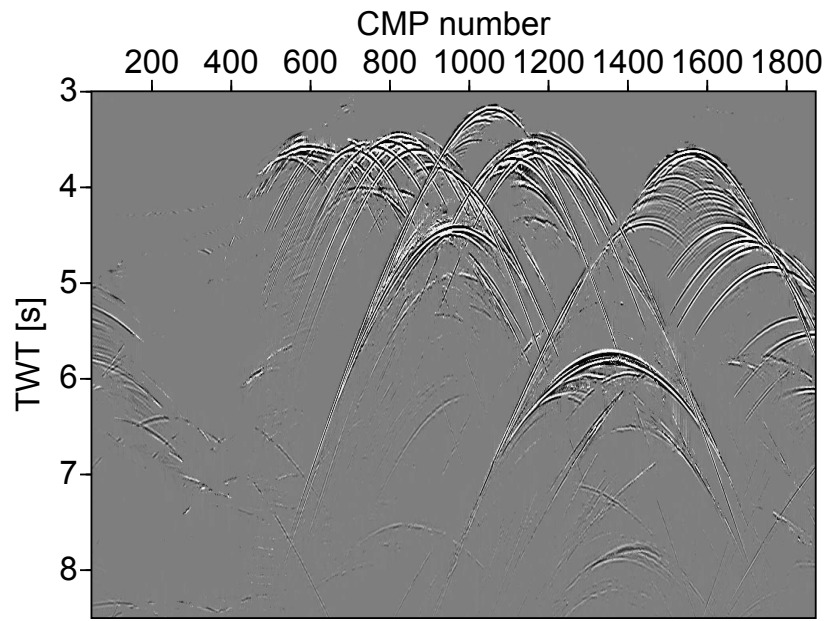


(b)

Figure 2: Sigsbee 2A data set: (a) the velocity model and (b) zero-offset section. Please note that the red frames in the lower figure indicate the location of the closeups in the following examples.



(a)



(b)

Figure 3: Sigsbee 2A: zero-offset diffraction-only data after (a) poststack and, (b) prestack diffraction separation.

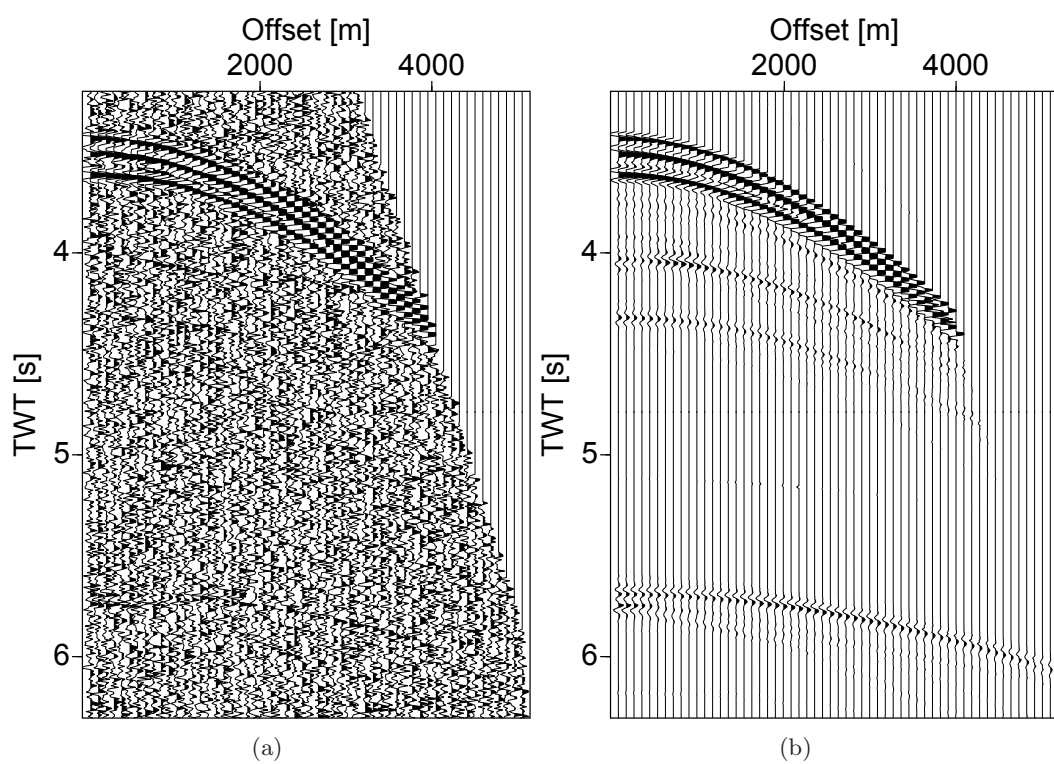


Figure 4: Sigsbee 2A: CMP 700 before (left) and after prestack diffraction separation (right).

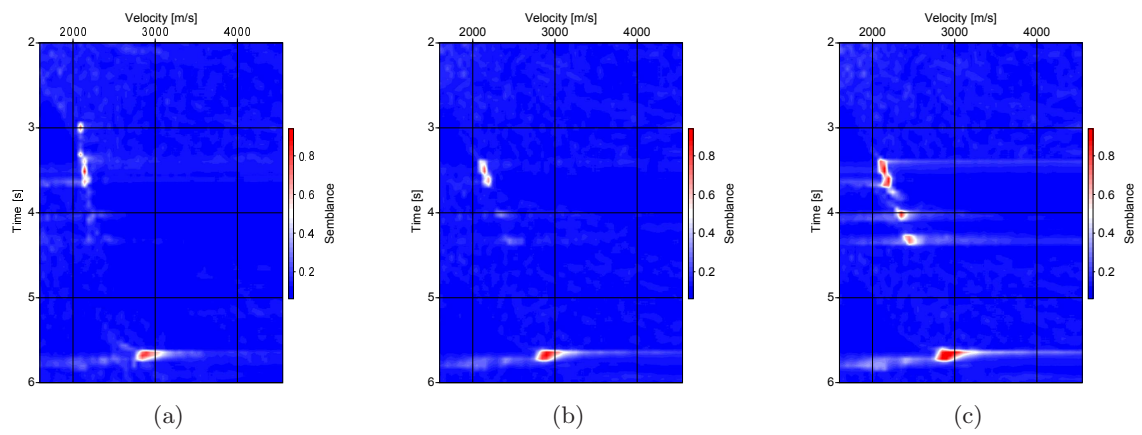


Figure 5: Sigsbee 2A: velocity spectrum for CMP 700, (a) before diffraction separation, (b) after poststack diffraction separation and (c) after prestack diffraction separation.

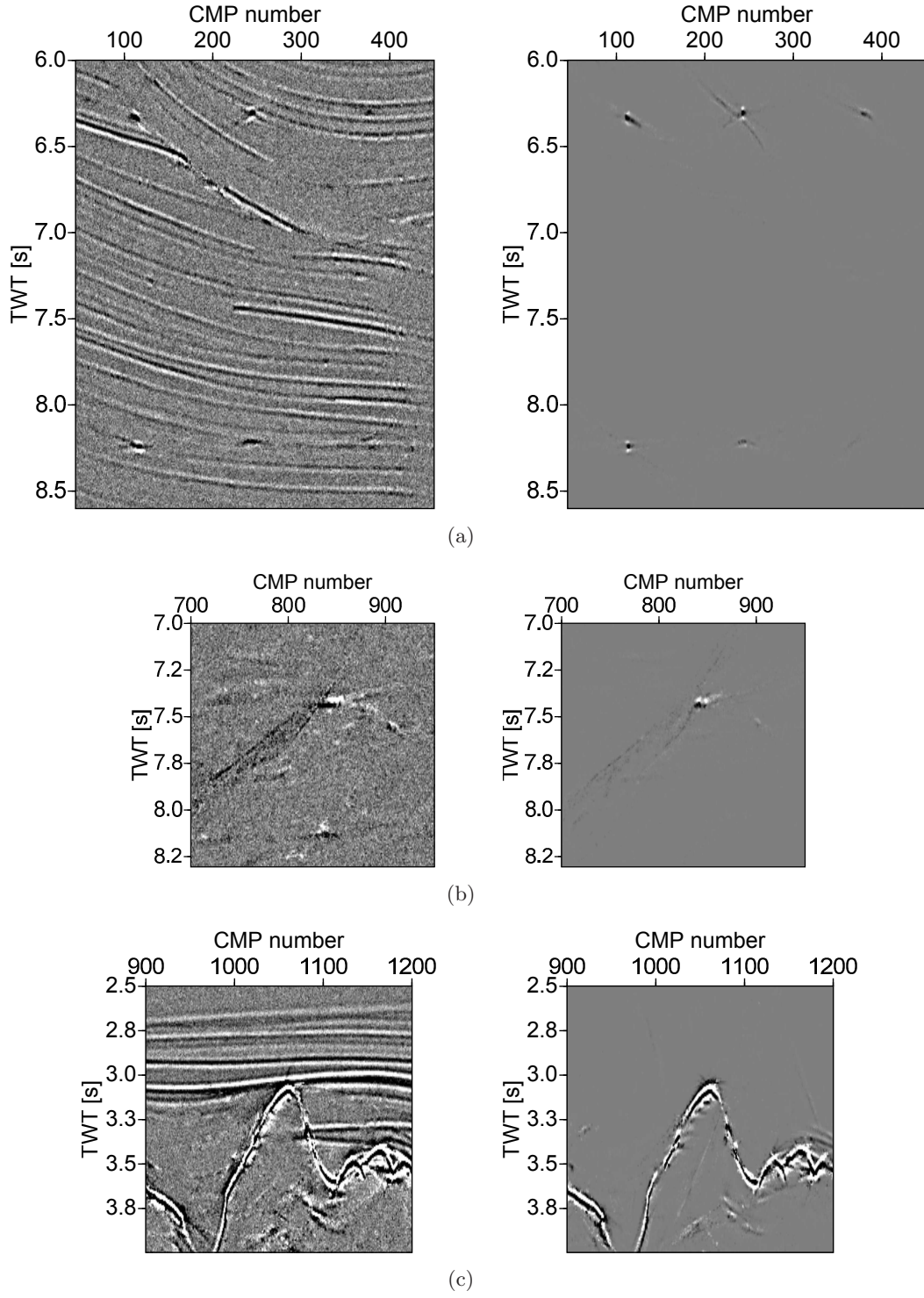


Figure 6: Sigsbee 2A: three closeup examples of time-migrated section of full (left) and diffraction-only data (right) from different regions of data. The locations of the closeups are indicated in the Figure 2(b).

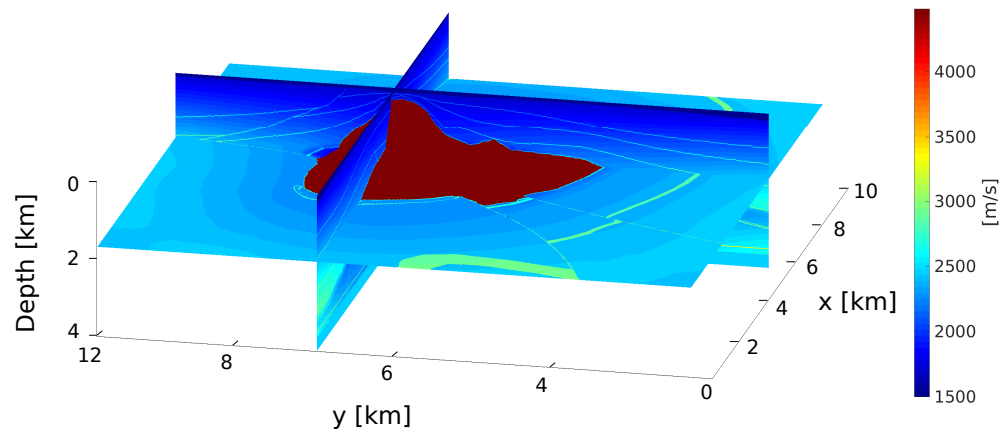


Figure 7: 3D SEG/EAGE velocity model of a salt body in the gulf of Mexico.

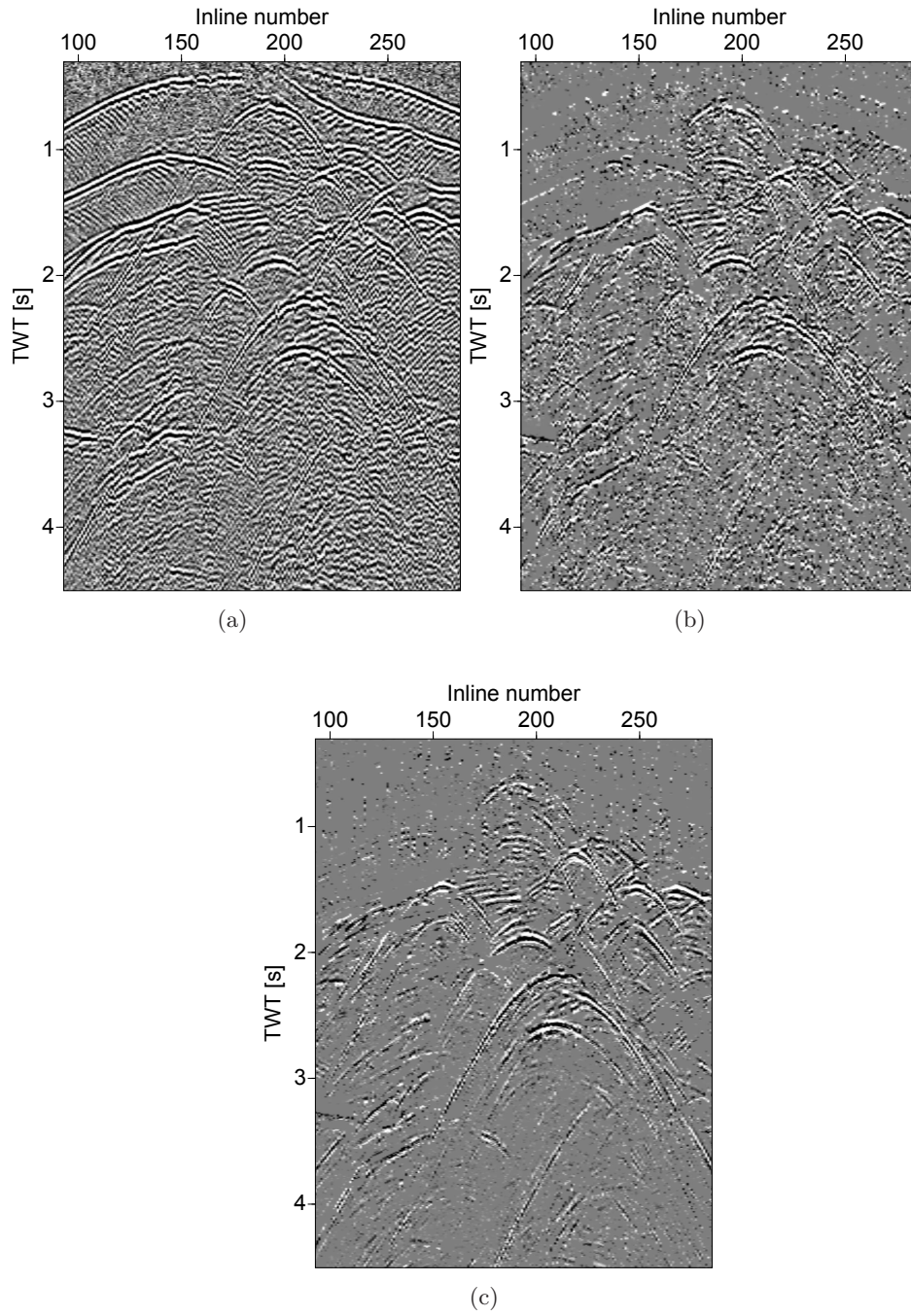


Figure 8: Crossline 300 of the 3D SEG/EAGE model: (a) stacked section prior to diffraction separation, zero-offset stack of diffraction-only data after (b) post- and (c) prestack diffraction separation.

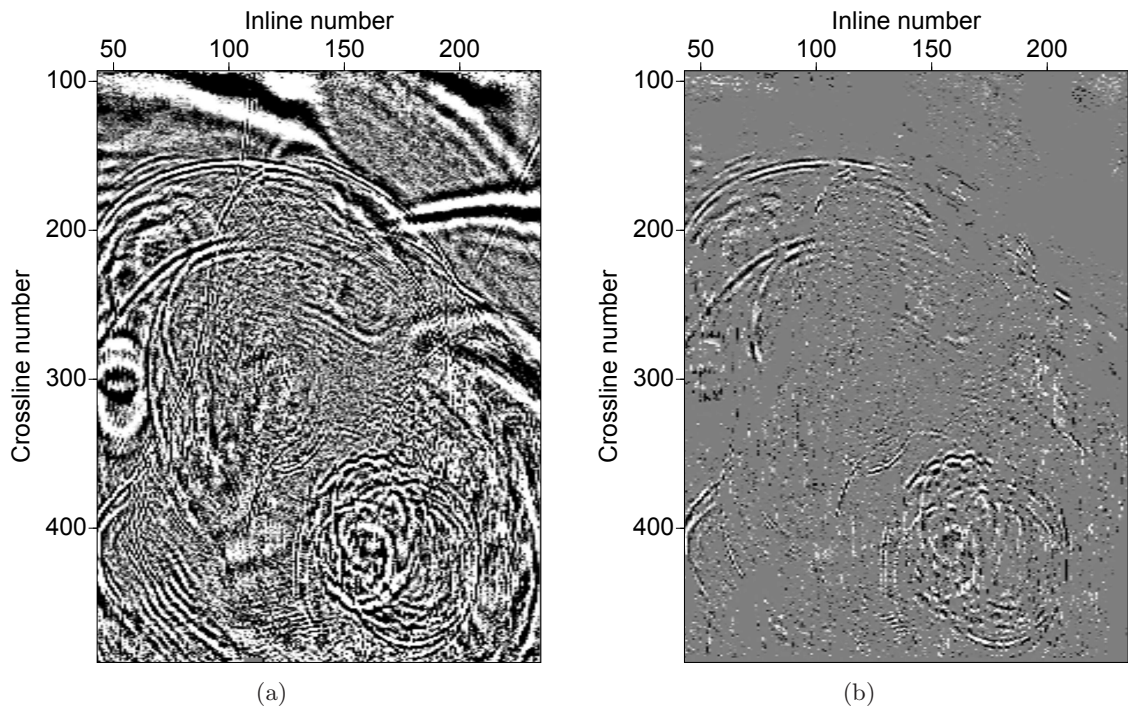


Figure 9: 3D SEG/EAGE model: time slice at 2.5 s, (a) stacked section prior to diffraction separation, (b) zero-offset stack of diffraction-only data after prestack diffraction separation. Please note that some residual reflections are present due to the lower threshold.

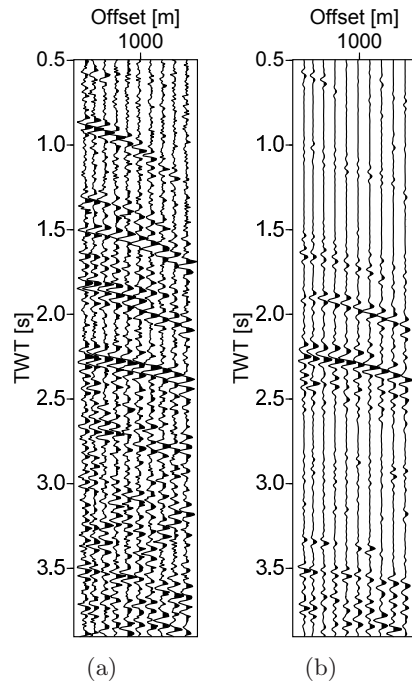


Figure 10: 3D SEG/EAGE model: results for a CMP gather at inline 130, (a) before and (b) after prestack diffraction separation.

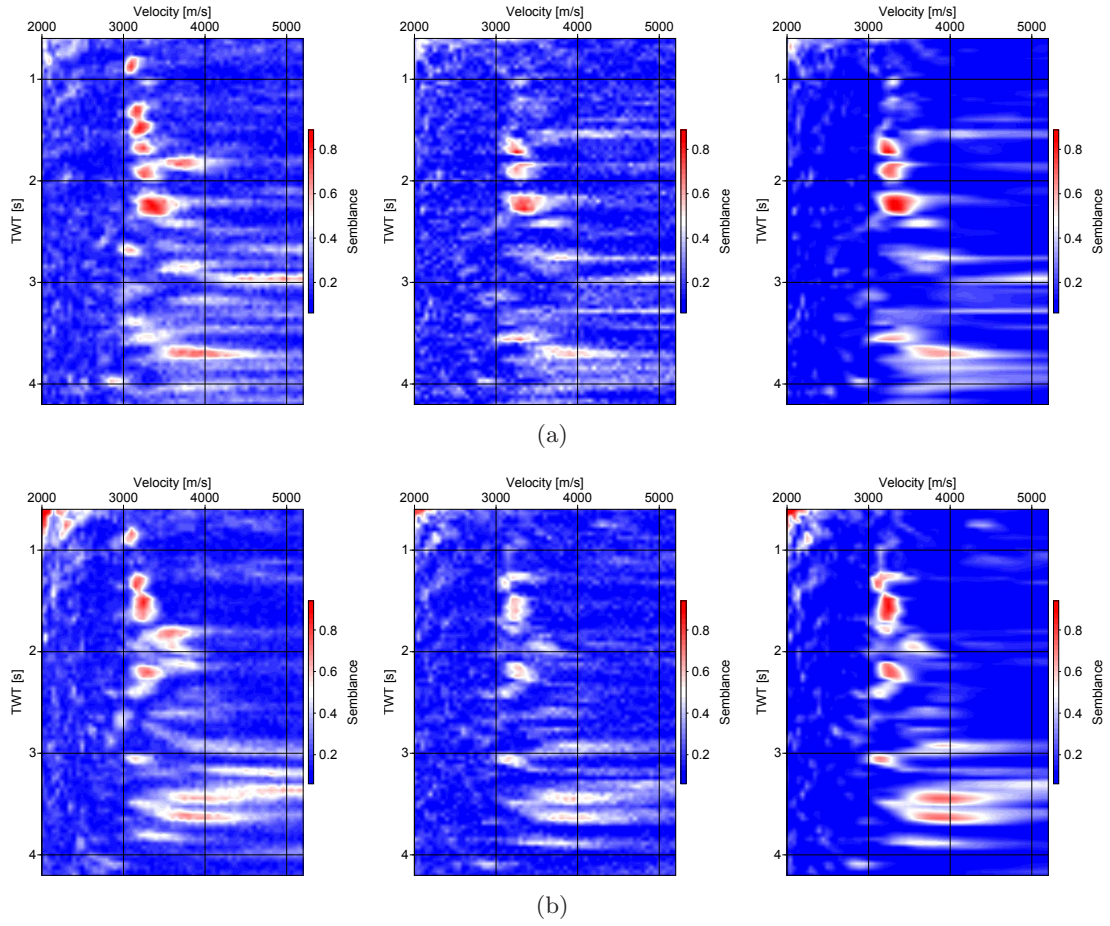


Figure 11: 3D SEG/EAGE model: top row show the velocity spectrum of a CMP gather at inline 130 before diffraction separation (left), after poststack diffraction separation (middle), and after prestack diffraction separation (right). Bottom row show the the velocity spectrum of a CMP gather at crossline 350 before diffraction separation (left), after poststack diffraction separation (middle), and after prestack diffraction separation (right).

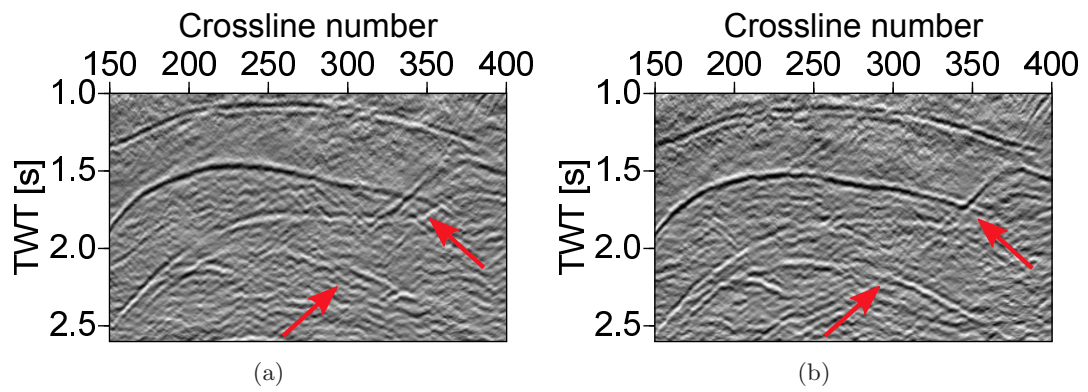


Figure 12: 3D SEG/EAGE model: prestack time migrated section using the velocity model obtained from data before (a) and after prestack diffraction separation (b) for inline 130. Red arrows indicate events that were better imaged by diffraction-only processing.

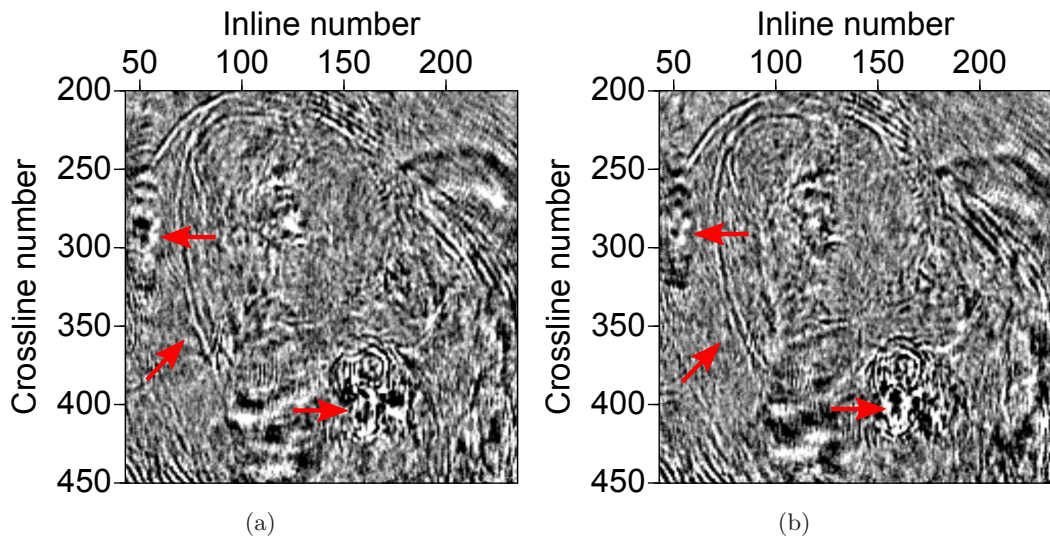


Figure 13: 3D SEG/EAGE model: time slice at 2.5 s, prestack time migrated image using the velocity model obtained from data (a) before and (b) after prestack diffraction separation. Red arrows indicate events that were better imaged by diffraction-only processing.